





Deformation response of highly stretchable and ductile graphene kirigami under uniaxial and biaxial tension

Pan Shi ¹, Yao Chen ^{1,*}, Ye Wei ², Jian Feng¹, Tong Guo¹, Yongming Tu¹ and Pooya Sareh ^{3,4}

¹Key Laboratory of Concrete and Prestressed Concrete Structures of Ministry of Education, Southeast University, Nanjing 211189, China

²School of Engineering, École Polytechnique Fédérale de Lausanne, Lausanne 1015, Switzerland

³Creative Design Engineering Lab (Cdel), Department of Mechanical and Aerospace Engineering, School of Engineering, University of Liverpool, Liverpool L69 3GH, United Kingdom

⁴School of Engineering, Newcastle University, Newcastle upon Tyne NE1 7RU, United Kingdom



(Received 6 June 2023; accepted 22 September 2023; published 9 October 2023)

Kirigami, the ancient technique of paper cutting, has been successfully applied to enhance the stretchability and ductility of nanoscale graphene. However, existing experimentally realized graphene kirigami (GK) are created by introducing parallel cuts, exhibiting exceptional mechanical properties in the direction perpendicular to the cuts but brittleness in the other direction. To overcome this limitation, we propose a fractal-cut GK with rotating triangular units, enabling high stretchability and ductility in both planar directions. We investigate the deformation response of this GK under uniaxial and biaxial tension using classic molecular dynamics simulations. The results demonstrate significant improvements compared with pristine graphene, with yield and fracture strains increased by more than 3 and 5 times, respectively, under uniaxial tension and by more than 3 and 4 times, respectively, under biaxial tension. Detailed analysis shows that high stretchability is attributed to the deformation mechanism of incision rotation and flipping, while high ductility is due to the deformation mechanism of incision rotation accompanied by ligament tearing. This configured GK is expected to open avenues into the design of flexible electronic devices at the nanoscale.

DOI: [10.1103/PhysRevB.108.134105](https://doi.org/10.1103/PhysRevB.108.134105)

I. INTRODUCTION

Graphene, a two-dimensional (2D) material with a thickness of only one atom, has attracted extensive interest among scientists and engineers over the last decade [1–3]. Due to extraordinary mechanical, thermal, and electronic properties [4–6], graphene has found a variety of potential applications such as nanocomposites [7], flexible electronics [8,9], nanomechanical resonators [10,11], DNA sequencing [12], gas separation [13], and water desalination [14,15]. When integrated into flexible and stretchable electronic devices, graphene generally undergoes continuous mechanical deformation, which may result in structural damage. Despite its extremely high stiffness and strength of ~ 1 Tpa and 100 GPa [4], graphene exhibits low ultimate strain and fractures immediately after yielding when subjected to stretching [16–18]. This brittle nature has somewhat limited the applications of graphene in flexible and stretchable electronic devices [19].

Kirigami, the ancient paper-cutting technique, has evolved into a design framework to engineer materials with desirable mechanical characteristics [20–24]. This technique has recently been experimentally demonstrated to dramatically enhance the stretchability and ductility of nanoscale graphene [25–27]. By introducing periodical parallel cuts, the yield and fracture strains of nanoscale monolayer graphene can be increased by more than a factor of three due to the

rotation-flipping deformation mechanism of the cuts [28–30]. Notably, this deformation mechanism only occurs when the edge cuts and interior cuts overlap [28]. Authors of further studies have demonstrated that the mechanical properties of graphene kirigami (GK) can be tailored controllably and predictably by tuning the geometry of the cuts [28,31,32]. Extreme stretchability of GK with certain dimensions can be achieved efficiently by utilizing machine learning and optimization algorithms [33–35].

However, GK with parallel cuts exhibit high stretchability and good ductility only in the direction normal to the cuts, while remaining brittle in the other planar direction. When subjected to combined loading conditions such as biaxial tension, this nanoarchitected kirigami metamaterial is prone to damage. Fractal-cut kirigami patterns, featuring rotating units, have been shown to impart high stretchability and ductility to 2D materials in both planar directions [36,37]. Using molecular dynamics (MD) simulations, Cai and Akbarzadeh [38] systematically investigated the thermomechanical properties of GK with rotating rectangular units and demonstrated the high stretchability of the investigated structure in both planar directions. They also realized the programmability of the stress-strain response and thermal conductivity for the GK by altering the incision geometry and introducing hierarchical cuts.

Inspired by the above studies, we apply a fractal-cut kirigami pattern with rotating triangular units [39], enabling the stretchability and ductility of macroscopic 2D structures in both planar directions, to nanoscale monolayer graphene.

*Corresponding author: chenyaoyao@seu.edu.cn

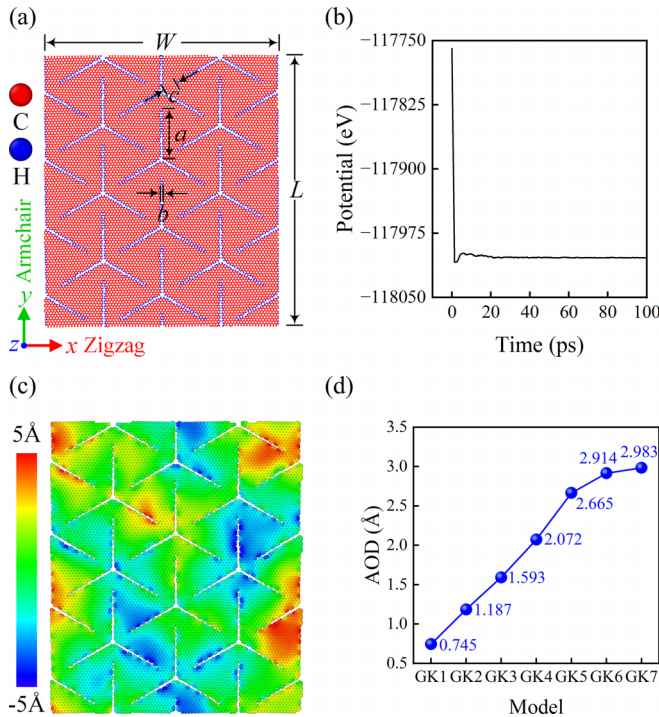


FIG. 1. (a) Schematic of graphene kirigami (GK), with key geometric parameters labeled. (b) Runtime-dependent potential energy profile of the representative GK. (c) Out-of-plane displacement nephogram of the representative GK after the thermal equilibration stage. (d) Average out-of-plane displacement (AOD) of various GK models. The model GK3 is the representative GK, and the incision sizes of the models are ranked as follows: GK1 < GK2 < GK3 < GK4 < GK5 < GK6 < GK7.

We employ classic MD simulations to systematically investigate the deformation response of the resulting GK under uniaxial and biaxial tension, which reveals the tensile deformation mechanism and the impact of incision geometry on the mechanical properties. We also introduce two dimensionless design parameters that can be utilized to controllably tailor the mechanical properties of GK. We expect that this configured kirigami can be applied to improve the stretchability and ductility of nanoscale graphene.

II. MODELS AND METHODS

The geometric configuration of GK with rotating triangular units is depicted in Fig. 1(a). Periodic radial incisions with an intersection angle of 120° are created in a graphene nanoribbon with dimensions of $L \times W$. The incision geometry is determined by three key parameters: the incision length a , the incision width b , and the ligament length c . Hydrogen atoms are added to form bonds with carbon atoms around the crack boundary to stabilize the incisions [38]. It should be noted that, in this paper, we only consider the case that incisions are parallel to the armchair (AC; y) direction. While the size of the GK changes according to the parametric analysis, a representative GK has 17 120 atoms, with $L = 221.56 \text{ \AA}$, $W = 191.88 \text{ \AA}$, $a = 42.61 \text{ \AA}$, $b = 2.46 \text{ \AA}$, and $c = 9.94 \text{ \AA}$. Our subsequent discussion on the deformation response of the kirigami structure under uniaxial and biaxial

tension is based on this specific geometry, and we then assess the relationship between mechanical properties and geometric parameters.

Our MD simulations are performed with the open-source code LAMMPS [40], and the software OVITO [41] is utilized to visualize the evolution of atomic structures. The AIREBO potential [42] is chosen to describe the C-C and C-H interatomic interactions, as this potential can accurately describe the bond breaking and reforming. In addition to the default potential parameters [42], the cutoff radius for the C-C bond is set as 2.0 \AA to avoid the spurious strengthening effect [43], and the cutoff radius for the Lennard-Jones term is set to 6.8 \AA [28]. Periodic boundary conditions are applied in the x and y directions to eliminate possible edge effects, while a nonperiodic and fixed boundary condition is adopted in the z direction. To adequately capture the out-of-plane deformation of GK during tension, the z -direction dimension of the simulation box is set to be much larger than the graphene thickness of 3.35 \AA [44].

In our MD simulations, the canonical NVT (constant atom number, volume, and temperature) ensemble [45,46] and the Verlet integrator [47] with a timestep of 1 fs are chosen. Initially, the GK is relaxed by conjugate gradient energy minimization with a tolerance of 10^{-10} . Subsequently, the system is relaxed at 4.2 K for 100 ps . This runtime is sufficient for the system to reach equilibrium, as demonstrated by the converged potential energy in Fig. 1(b). During the thermal equilibration stage, we observe the atomistic structure of GK rippling out-of-plane [Fig. 1(c)], with the ripple amplitude [i.e., average out-of-plane displacements (AODs) of all C atoms with respect to their respective initial positions] increasing in correlation with the incision size [Fig. 1(d)]. This ripple phenomenon stems from the local buckling of the structure triggered by the incision defects, which has also been observed in MD simulations of GK with different cutting patterns [31,38,43,48,49]. Finally, the deformation-control method [50,51] is adopted to perform the uniaxial and biaxial tensile tests of the GK. To save computational time, we choose a particular strain rate of 0.01 ps^{-1} , as strain rate exerts a limited impact on the fracture strain and fracture strength of graphene at low temperatures [44]. The tensile stress is calculated as the stress parallel to the loading direction times the z -direction dimension of the simulation box and divided by the graphene effective thickness [33]. The calculated tensile stress is averaged every 100 timesteps to obtain a relationship between stress and strain. Additionally, atomic trajectories are recorded at the same intervals to visualize the transformations of atomic structures.

III. RESULTS AND DISCUSSIONS

A. Deformation response under uniaxial and biaxial tension

We first investigate the deformation response of the representative GK under uniaxial tension in the AC direction. To illustrate the deformation response, we show the tensile stress-strain curve in Fig. 2(a) along with a series of atomic snapshots in Fig. 2(c). Additionally, the AOD and the number of C-C bonds vs strain are plotted in Fig. 2(b). The AOD is calculated by averaging the z -direction displacements of all C atoms with respect to their positions prior to loading. We

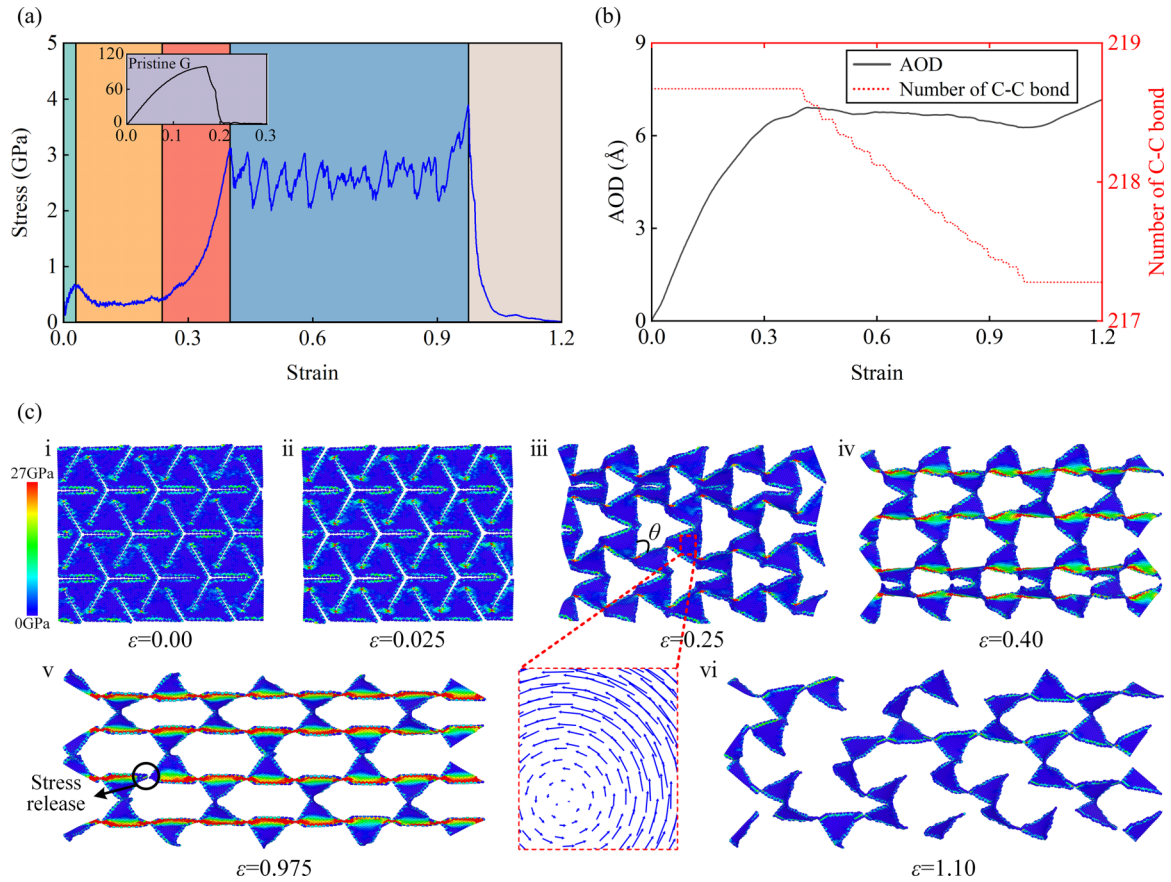


FIG. 2. (a) Stress-strain curve of the representative graphene kirigami (GK) under uniaxial tension in the armchair direction. Green, yellow, orange, blue, and gray regions correspond to five stages of deformation. A stress-strain curve of a pristine armchair graphene nanoribbon with the same size is depicted in the inset for comparison. (b) Average out-of-plane displacement (AOD) and number of C-C bonds as functions of strain. (c) Von Mises stress distribution of the representative GK at different deformation stages. The displacement of carbon atoms shown by vector arrows on each atom indicates the rotation of the domains during the initial tensile process. θ is the in-plane rotation angle of the incisions.

take a cutoff radius of 2 \AA to determine the formation of C-C bonds.

Figure 2(a) shows that the deformation response of GK is divided into five distinct stages. Before tensile strain is applied, as shown in Fig. 2(c)(i), a certain degree of residual stress is produced around the crack boundary due to the use of the NVT ensemble [28,52]. Once the atomic structure is stretched, the interior incisions simultaneously rotate in-plane and flip out-of-plane, as indicated by the vector arrows in Fig. 2(c) and the AOD in Fig. 2(b), respectively. In the initial loading stage (green region), the tensile stress increases sharply until the atoms around the crack tips yield [Fig. 2(c)(ii)]. After that, in-plane rotation and out-of-plane flipping continue, whereas atomic yielding does not develop, as shown in Fig. 2(c)(iii). As a result, the stress-strain curve exhibits a long plateau that sustains up to a strain of ~ 0.25 (yellow region). During these two stages, the structure is deformed without significantly stretching carbon bonds.

However, when the incisions are rotated at a certain angle, the carbon bonds begin to be stretched, accompanied by the yielding of the atoms around the crack tips. As such, local high-stress regions are induced around the crack tips and gradually progress toward the internal structure, as shown in Fig. 2(c)(iv). This leads to a rapid increase in structural

stress until a strain of 0.40 is reached (orange region). This strain indicates the global yielding of the atomic structure. We observe from Fig. 2(b) that, at this yield strain, the out-of-plane flipping has reached its limit, and the carbon bonds begin to break. Therefore, incision rotation and flipping are the main deformation behavior prior to the global yielding of the structure.

After global yielding, the ligaments are progressively torn because of structure elongation accompanied by incision rotation. The C-C bonds around the crack tips experience severe disruption, which occurs in stages, as manifested by the zigzag download dashed line in Fig. 2(b). The bond breakage results in a drop in stress, after which the stress increases again due to the stretching of the C-C bonds around the newly created crack tips. Consequently, the tensile stress exhibits fluctuations, as illustrated by the orange region in Fig. 2(a). At this stage, as shown in Fig. 2(c)(v), high-stress regions between neighboring triangular units are connected to form narrow bands. Once the ligaments are ruptured, the stresses within them are released. The increasing rotation angle θ demonstrates that incision rotation and ligament tearing are the primary deformation behavior at this stage. The ligament tearing causes the narrow stress bands to disappear, signifying complete fracture of the GK structure [Fig. 2(c)(vi)].

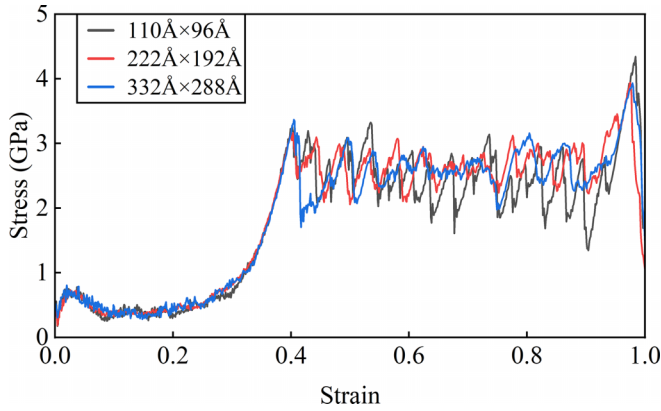


FIG. 3. Armchair tension stress-strain curves for graphene kirigami with the same triangular unit and different sample size.

We note that the yield stress of the GK is reduced by an order of magnitude compared with pristine graphene, while the yield and fracture strains are increased by more than factors of two (from 0.17 to 0.40) and five (from 0.17 to 0.98), respectively. The substantial increase in fracture strain suggests extremely enhanced stretchability of GK, while the postyielding elongation of $>50\%$ demonstrates good ductility of the kirigami structure. The high stretchability is attributed to the deformation mechanism of incision rotation and flipping, while the high ductility results from the deformation mechanism of incision rotation accompanied by ligament tearing. As discussed in the introduction, GK with rotating rectangular units is also highly stretchable. Nevertheless, MD simulations by Cai and Akbarzadeh [38] demonstrate an AC fracture strain of ~ 0.4 for this GK, which is less than half of our simulations. This indicates that rotating triangle kirigami can endow nanoscale graphene with superior stretchability compared with rotating rectangle kirigami.

To explore how much the size of the models can influence the results, we construct two other GK models with the same triangular unit and different sample dimensions. As shown in Fig. 3, the preyielding curves for the three models almost coincide. Although the fluctuation stages are different, the yield strain, yield stress, fracture strain, and fracture stress of the three models are basically the same. Therefore, the size of $222 \times 192 \text{ \AA}$ can provide accurate and reliable simulation results.

The stress-strain curves for the AC and ZZ GK are shown in Fig. 4. These curves exhibit a similar trend, with the deformation response divided into five distinct stages. The initial two stages largely overlap, suggesting the same deformation mechanism in both directions. However, in comparison with the AC graphene, the ZZ graphene enters yielding later and experiences earlier fracture, indicating that the AC graphene has higher stretchability and ductility than the ZZ graphene. That is, the mechanical properties of GK are sensitive to the loading direction. Generally, this configured kirigami pattern considerably enhances the stretchability and ductility of graphene in the planar directions.

Having demonstrated the high stretchability and ductility of GK, we further investigate its deformation response under biaxial tension. Similarly, as shown in Fig. 5(a), the stretch-

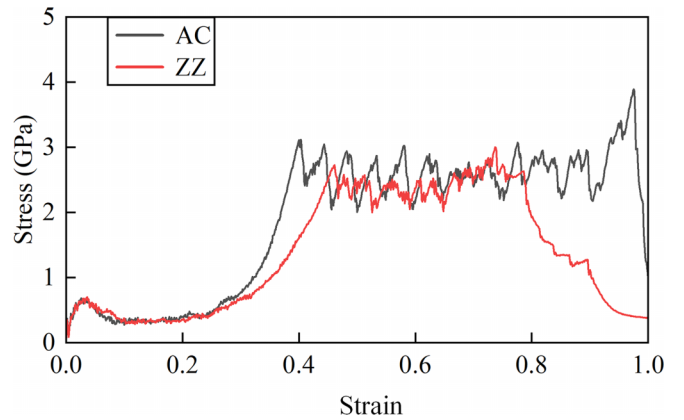


FIG. 4. Stress-strain curves of the representative graphene kirigami under uniaxial tension along the armchair (AC) and zigzag (ZZ) directions.

ability and ductility of graphene are significantly enhanced under biaxial tension. The yield and fracture strains are increased by more than twice and four times, respectively, and the GK can sustain $>40\%$ elongation after yield. However, the deformation behavior of GK slightly differs from that under uniaxial tension. As shown in Fig. 5(b), the AOD increases sharply in the first two stages and decreases afterward, which diverges from the curve trend in Fig. 2(b). We observe an abrupt change in the decline rate at the yield point, ascribed to the newly created crack surfaces triggered by ligament tearing. Interestingly, as depicted in Fig. 5(b)(i), the atoms around the ligament are folded to form a tetrahedron, while the internal atoms remain in a plane parallel to the z direction. This deformation behavior resembles that of macroscopic kirigami structures under uniaxial tension [53]. Additionally, the high-stress regions are concentrated around the ligaments, consistent with finite element results of macroscopic kirigami [39,53,54].

B. Influence of incision geometry on mechanical properties

Having demonstrated that the proposed kirigami pattern can significantly enhance the stretchability and ductility of graphene in both planar directions, we further systematically investigate the effect of the incision geometry in Fig. 1(a) on the mechanical properties of GK. Understanding this effect can enable the design of GK with desirable mechanical properties. To this end, an additional six models with the same sample size (L and W) and different incision geometries (a , b , and c) are constructed, as listed in Table I. Among these models, GK3 is the representative GK; GK1, GK2, GK3, and

TABLE I. Incision geometry parameters for the studied GK models.

	GK1	GK2	GK3	GK4	GK5	GK6	GK7
a (Å)	34.09	38.35	42.61	46.87	42.61	42.61	42.61
b (Å)	2.46	2.46	2.46	2.46	4.92	7.38	9.64
c (Å)	18.46	14.20	9.94	5.68	8.52	8.52	5.68

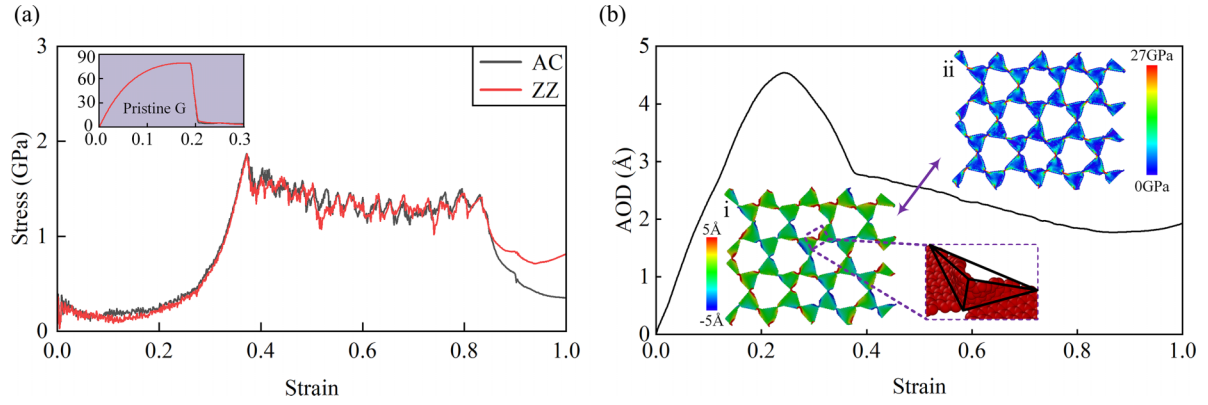


FIG. 5. (a) Armchair (AC) and zigzag (ZZ) stress-strain curves of the representative graphene kirigami under biaxial tension. A stress-strain curve of a pristine graphene nanoribbon with the same size is depicted in the inset for comparison. (b) Average out-of-plane displacement (AOD) as a function of strain. (i) Out-of-plane displacement nephogram and (ii) von Mises stress distribution at a strain of 0.5 are depicted in the inset.

GK4 have an identical incision width with varying ligament length; GK3, GK5, GK6, and GK7 have an equal incision length with varying incision width. To characterize the impact of incision geometry on the mechanical properties, we introduce two dimensionless parameters: $\alpha = a/(a + c)$ and $\beta = b/(a + c)$.

Figure 6 depicts the stress-strain curves for various GK models subjected to uniaxial tension. It can be observed that the incision geometry significantly impacts the mechanical response of GK. In Figs. 6(a) and 6(c), an increase in α results in weaker mechanical responses in the initial two stages, a longer curve plateau, and a larger yield strain. This is attributed to the

enhanced incision rotation-flip mechanism caused by more linear defects. In addition, we observe that decreasing α leads to a higher ductility, which is because new crack surfaces created by the ligament tearing can rotate and flip. Despite this superior performance, the ligament tearing means that the structure begins to break down, which hampers its practical application. In Figs. 6(b) and 6(d), increasing β yields similar results to increasing α . However, the initial peak almost disappears with increasing β , indicating that a wider incision can weaken the stress concentration around the crack tip. Note that the stress-strain curves in both directions are qualitatively similar but quantitatively different. This discrepancy primarily arises from the sensitivity of the deformation response to the loading direction, which is caused by the incision geometry.

The advantages of GK over pristine graphene lie in its high stretchability and ductility. To quantitatively assess how the incision geometry impacts these two characteristics, we extract the yield strain and the fracture strain from the stress-strain curves, as shown in Fig. 7. Additionally, we calculate the Young's modulus of GK, as listed in Table II. According to the nature of the stress-strain curve in Fig. 2(a), we determine two Young's moduli E_1 and E_2 by linearly fitting the curves in the first and third stages.

As shown in Fig. 7, the yield strain increases by a maximum of 3.6 times, while the fracture strain increases by a maximum of 5.7 times. Both yield and fracture strains show a linear increase with α , while increasing β leading to a linear increase in yield strain but a decrease in fracture strain. To ensure that the structure does not suffer local damage (i.e., torn ligaments) under tension, GK should have as high a yield strain as possible. This means that α and β should take on

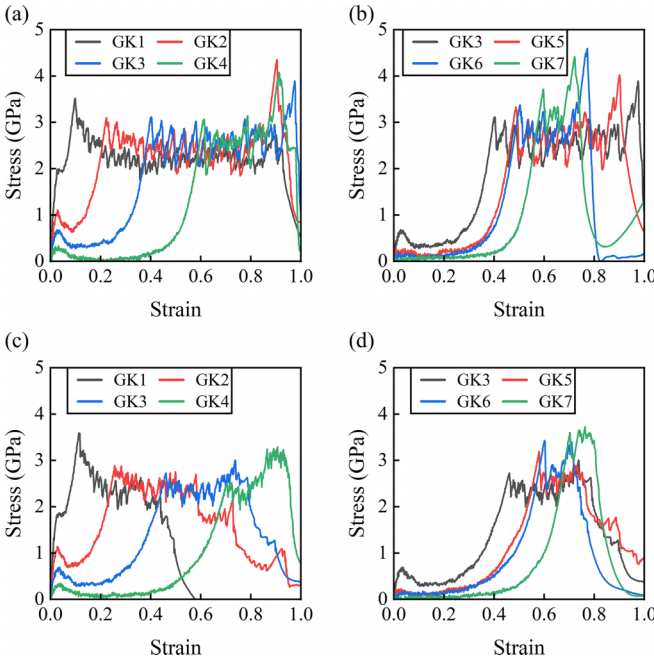


FIG. 6. Stress-strain curves for different graphene kirigami (GK) models under uniaxial tension. (a) and (b) armchair direction; (c) and (d) zigzag direction. GK1, GK2, GK3, and GK4 have an identical incision width with increasing α , while GK3, GK5, GK6, and GK7 have an equal incision length with increasing β .

TABLE II. Young's modulus (E) for different GK models.

E (GPa)	GK1	GK2	GK3	GK4	GK5	GK6	GK7
E_1 (AC)	67.7	33.2	20.1	8.3	2.6	1.08	0.9
E_2 (AC)	35.4	28.6	27.1	26.3	28.4	29.4	31.3
E_1 (ZZ)	63.2	35.24	14.7	6.1	3.82	3.1	0.8
E_2 (ZZ)	32.9	24.3	16.3	15.0	19.9	22.3	26.0

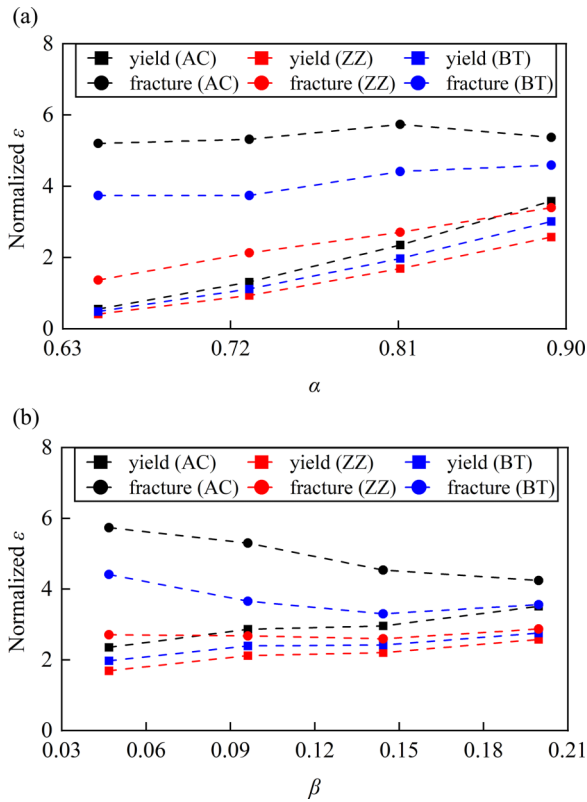


FIG. 7. Influence of (a) α and (b) β on the yield strain and the fracture strain of graphene kirigami under uniaxial and biaxial tension (BT). Data are normalized by simulation results of a pristine graphene nanoribbon with the same size.

larger values. However, our MD simulations indicate that GK with extremely large α or β may curl during the thermal equilibrium stage. Therefore, rational design of the incision geometry is essential to achieve GK with high stretchability and ductility.

Table II lists the Young's moduli for both AC and ZZ GK. The Young's modulus of GK is significantly lower than that of pristine graphene (~ 900 GPa). Additionally, increasing α weakens the Young's moduli of both stages, while increasing β reduces the first-stage Young's modulus (E_1) but enhances the second-stage modulus (E_2).

IV. CONCLUSIONS

We have utilized MD simulations to systematically investigate the deformation responses of nanoscale GK with rotating triangular units under uniaxial and biaxial tension. The proposed GK have been demonstrated to possess high stretchability and ductility in both planar directions. Especially under biaxial tension, the GK can possess a yield strain of more than twice that of pristine graphene, along with a fracture strain of more than four times. The high stretchability arises from the deformation mechanism of incision rotation and flipping, while the high ductility is attributed to the deformation mechanism of incision rotation accompanied by ligament tearing.

Furthermore, we have examined the impact of the incision geometry on the mechanical properties of GK. Two key geometric parameters (α and β) have been identified to tailor the mechanical properties of GK controllably. It is found that an increase in α or β enhances stretchability but reduces ductility. To further establish the nonlinear relationship between the identified geometric parameters and the target properties, it is necessary to increase the model size and enrich the cutting patterns (e.g., nonperiodic patterns). However, this will significantly increase the computational cost. Based on the established relationship, the inverse design of GK with desirable mechanical properties can be realized with the help of analytical and numerical algorithms [33–35,55].

Overall, we expect that this configured kirigami pattern can effectively mitigate the brittle nature of nanoscale graphene and other 2D nanomaterials. Additionally, this kirigami pattern can be extended to tune the thermal [38,56] and electronic [29,49] properties of graphene, further expanding its potential applications.

ACKNOWLEDGMENTS

This paper has been supported by the National Natural Science Foundation of China (Grants No. 51978150 and No. 52050410334), the Fundamental Research Funds for the Central Universities, and the Postgraduate Research & Practice Innovation Program of Jiangsu Province (No. SJCX23_0071). Y.C. would like to acknowledge financial support from the Alexander von Humboldt-Foundation for his academic research at Max-Planck-Institut für Eisenforschung GmbH, Germany.

- [1] A. G. Olabi, M. A. Abdelkareem, T. Wilberforce, and E. T. Sayed, *Renew. Sustain. Energy Rev.* **135**, 110026 (2021).
- [2] A. K. Geim and K. S. Novoselov, *Nat. Mater.* **6**, 183 (2007).
- [3] N. Rohaizad, C. C. Mayorga-Martinez, M. Fojtu, N. M. Latiff, and M. Pumera, *Chem. Soc. Rev.* **50**, 619 (2021).
- [4] C. Lee, X. Wei, J. W. Kysar, and J. Hone, *Science* **321**, 385 (2008).
- [5] A. A. Balandin, S. Ghosh, W. Z. Bao, I. Calizo, D. Teweldebrhan, F. Miao, and C. N. Lau, *Nano Lett.* **8**, 902 (2008).
- [6] Y. B. Zhang, Y. W. Tan, H. L. Stormer, and P. Kim, *Nature (London)* **438**, 201 (2005).
- [7] T. Ramanathan, A. A. Abdala, S. Stankovich, D. A. Dikin, M. Herrera-Alonso, R. D. Piner, D. H. Adamson, H. C. Schniepp, X. Chen, and R. S. Ruoff, *Nat. Nanotechnol.* **3**, 327 (2008).
- [8] K. S. Kim, Y. Zhao, H. Jang, S. Y. Lee, J. M. Kim, K. S. Kim, J. H. Ahn, P. Kim, J. Y. Choi, and B. H. Hong, *Nature (London)* **457**, 706 (2009).
- [9] M. F. El-Kady, V. Strong, S. Dubin, and R. B. Kaner, *Science* **335**, 1326 (2012).
- [10] C. Y. Chen, S. Rosenblatt, K. I. Bolotin, W. Kalb, P. Kim, I. Kymissis, H. L. Stormer, T. F. Heinz, and J. Hone, *Nat. Nanotechnol.* **4**, 861 (2009).

- [11] A. Voje, J. M. Kinaret, and A. Isacson, *Phys. Rev. B* **85**, 205415 (2012).
- [12] G. F. Schneider, S. W. Kowalczyk, V. E. Calado, G. Pandraud, H. W. Zandbergen, L. Vandersypen, and C. Dekker, *Nano Lett.* **10**, 3163 (2010).
- [13] H. W. Kim, H. W. Yoon, S. M. Yoon, B. M. Yoo, B. K. Ahn, Y. H. Cho, H. J. Shin, H. Yang, U. Paik, and S. Kwon, *Science* **342**, 91 (2013).
- [14] D. Cohen-Tanugi and J. C. Grossman, *Nano Lett.* **12**, 3602 (2012).
- [15] J. Liu, G. S. Shi, P. Guo, J. R. Yang, and H. P. Fang, *Phys. Rev. Lett.* **115**, 164502 (2015).
- [16] F. Liu, P. Ming, and J. Li, *Phys. Rev. B* **76**, 064120 (2007).
- [17] M. Xu, J. T. Paci, J. Oswald, and T. Belytschko, *Int. J. Solids Struct.* **49**, 2582 (2012).
- [18] H. Zhao, and K. Min, and N. R. Aluru, *Nano Lett.* **9**, 3012 (2009).
- [19] H. Jang, Y. J. Park, X. Chen, T. Das, M. S. Kim, and J. H. Ahn, *Adv. Mater.* **28**, 4184 (2016).
- [20] J. Tao, H. Khosravi, V. Deshpande, and S. Li, *Adv. Sci.* **10**, 2204733 (2023).
- [21] Y. Chen, P. Shi, Y. Bai, J. Li, J. Feng, and P. Sareh, *Thin Walled Struct.* **185**, 110572 (2023).
- [22] Z. Zhang, Z. Tian, Y. Mei, and Z. Di, *Mater. Sci. Eng.: R: Rep.* **145**, 100621 (2021).
- [23] Y. Chen, R. Xu, C. Lu, K. Liu, J. Feng, and P. Sareh, *Int. J. Mech. Sci.* **247**, 108196 (2023).
- [24] Z. Zhai, L. Wu, and H. Jiang, *Appl. Phys. Rev.* **8**, 41319 (2021).
- [25] M. K. Blees, A. W. Barnard, P. A. Rose, S. P. Roberts, K. L. McGill, P. Y. Huang, A. R. Ruyack, J. W. Kevek, B. Kobrin, D. A. Muller *et al.*, *Nature (London)* **524**, 204 (2015).
- [26] K. Xu, Y. Lu, S. Honda, T. Arie, S. Akita, and K. Takei, *J. Mater. Chem. C* **7**, 9609 (2019).
- [27] K. Yong, S. De, E. Y. Hsieh, J. Leem, N. R. Aluru, and S. Nam, *Mater. Today* **34**, 58 (2020).
- [28] Z. Qi, D. K. Campbell, and H. S. Park, *Phys. Rev. B* **90**, 245437 (2014).
- [29] B. Mortazavi, A. Lherbier, Z. Fan, A. Harju, T. Rabczuk, and J. Charlier, *Nanoscale* **9**, 16329 (2017).
- [30] Z. Hua, Y. Zhao, S. Dong, P. Yu, Y. Liu, N. Wei, and J. Zhao, *Soft Matter* **13**, 8930 (2017).
- [31] B. Zheng and G. X. Gu, *Carbon* **155**, 697 (2019).
- [32] S. Dong, Y. Xia, R. Huang, and J. Zhao, *Carbon* **158**, 77 (2020).
- [33] P. Z. Hanakata, E. D. Cubuk, D. K. Campbell, and H. S. Park, *Phys. Rev. Lett.* **121**, 255304 (2018).
- [34] P. Z. Hanakata, E. D. Cubuk, D. K. Campbell, and H. S. Park, *Phys. Rev. Res.* **2**, 042006(R) (2020).
- [35] P. Rajak, B. Wang, K. Nomura, Y. Luo, A. Nakano, R. Kalia, and P. Vashishta, *npj Comput. Mater.* **7**, 102 (2021).
- [36] Y. Sun, W. Ye, Y. Chen, W. Fan, J. Feng, and P. Sareh, *Structures* **33**, 3633 (2021).
- [37] E. Jalali, H. Soltanizadeh, Y. Chen, Y. M. Xie, and P. Sareh, *Commun. Mater.* **3**, 97 (2022).
- [38] J. Cai and A. Akbarzadeh, *Mater. Design* **206**, 109811 (2021).
- [39] Y. Chen, W. Ye, R. Xu, Y. Sun, J. Feng, and P. Sareh, *Int. J. Mech. Sci.* **249**, 108249 (2023).
- [40] A. P. Thompson, H. M. Aktulga, R. Berger, D. S. Bolintineanu, W. M. Brown, P. S. Crozier, P. J. I. Veld, A. Kohlmeyer, S. G. Moore, T. D. Nguyen *et al.*, *Comput. Phys. Commun.* **271**, 108171 (2022).
- [41] A. Stukowski, *Modelling Simul. Mater. Sci. Eng.* **18**, 15012 (2010).
- [42] S. J. Stuart, and A. B. Tutein, and J. A. Harrison, *J. Chem. Phys.* **112**, 6472 (2000).
- [43] O. A. Shenderova, D. W. Brenner, A. Omeltchenko, X. Su, and L. H. Yang *Phys. Rev. B* **61**, 3877 (2000).
- [44] H. Zhao and N. R. Aluru, *J. Appl. Phys.* **108**, 64321 (2010).
- [45] S. Nosé, *J. Chem. Phys.* **81**, 511 (1984).
- [46] W. G. Hoover, *Phys. Rev. A* **31**, 1695 (1985).
- [47] L. Verlet, *Phys. Rev.* **159**, 98 (1967).
- [48] B. F. Grosso and E. J. Mele, *Phys. Rev. Lett.* **115**, 195501 (2015).
- [49] D. A. Bahamon, Z. Qi, H. S. Park, V. M. Pereira, and D. K. Campbell, *Phys. Rev. B* **93**, 235408 (2016).
- [50] N. Wei, L. Xu, H. Wang, and J. Zheng, *Nanotechnology* **22**, 105705 (2011).
- [51] Y. Tu, P. Shi, D. Liu, R. Wen, Q. Yu, G. Sas, and L. Elfgren, *Phys. Chem. Chem. Phys.* **24**, 1156 (2022).
- [52] Y. Gao and B. Xu, *Acs Nano* **12**, 11254 (2018).
- [53] Y. Tang, Y. Li, Y. Hong, S. Yang, and J. Yin, *Proc. Natl. Acad. Sci. USA* **116**, 26407 (2019).
- [54] Y. Cho, J. H. Shin, A. Costa, T. A. Kim, V. Kunin, J. Li, S. Y. Lee, S. Yang, H. N. Han, I. S. Choi *et al.*, *Proc. Natl. Acad. Sci. USA* **111**, 17390 (2014).
- [55] Z. Rao, P. Y. Tung, R. W. Xie, Y. Wei, H. B. Zhang, A. Ferrari, T. P. C. Klaver, F. Kormann, P. T. Sukumar, A. K. da Silva *et al.*, *Science* **378**, 78 (2022).
- [56] N. Wei, Y. Chen, K. Cai, J. Zhao, H. Wang, and J. Zheng, *Carbon* **104**, 203 (2016).